

Hydrodynamic Implosion Simulation Including Relativistic Effects on Petawatt-Class Pulse Heating

Mitsuru Honda

Plasma Astrophysics Laboratory, Institute for Global Science, Mie 519-5203, Japan

Abstract

A spherically symmetric fluid code that includes the relativistic effects of hot electrons has been newly developed. In the present simulations, I attempt to implode a target shell of laser fusion using a nanosecond pulse; then, an additional heating short pulse is injected into the coronal plasma surrounding a highly compressed core. I found that the relativistic effects of hot electrons on electron transport are likely to inhibit the heat flows, and to reduce thermonuclear fusion neutrons significantly. This feature may be important for off-center fast ignition and burn of fusion targets.

KEYWORDS: fusion, laser fusion, fast ignition, fluid simulation, electron transport, relativistic effects

The relativistic effects of hot electrons in laboratory plasmas have attracted much interests for the past decades [1], particularly, relating to laser fusion fast ignition (LFFI) whose scenario is achieved by standard high-compression, irradiation of a hole-boring laser beam, irradiation of an ignitor laser beam, and thermonuclear burn [2]. When high-intensity short pulse laser light is impinged on the coronal plasma surrounding a highly compressed core in the 'hole-boring' and 'ignition' stages, energetic particles are sprayed through various mechanisms. In order to investigate the relativistic electron transport carrying huge currents, substantial studies were performed on the multidimensional relativistic particle-in-cell [3] as well as magneto-hydrodynamic [4] simulations.

Moreover, the fast ignition conditions of the compressed targets have been presented in some publications [5, 6, 7, 8]. Indeed, it is important to survey the energy transport and relaxation in dense plasmas over a large spatiotemporal system of $R > 10^1 - 10^2 \mu\text{m}$ and $t > 1 \text{ ps}$. Concerning the extension of the analysis of ignition conditions, we are now strongly encouraged to improve the transport coefficients so as to compare them with those for kinetic simulations [9, 10] and experiments [11, 12]. That is why, I attempted to construct a computational fluid code that includes relativistic effects of electron transport. In this code, the transport properties of hot electrons are fully consistent with the current-neutral electric fields self-induced in plasmas, as discussed in ref. [13] in detail.

In this paper, I argue that in the context of the LFFI, heat flux inhibition owing to relativistic effects of electrons degrades the transport efficiency of deflagration thermal waves, and leads to some reductions in the neutron yields. This is essentially because the drift velocity carrying heat asymptotically approaches the speed of light. Since the velocity moment of the heat flux is large, the energy of electrons carrying dominant heat (EE-CDH) is much larger than the thermal energy: $T_{\text{EE-CDH}} \approx 7T_{\text{th}}$. Thus, it is expected that the relativistic effects of electron heat transport can be observed even in the energy domain of $T_{\text{th}} \sim 10^1 - 10^2 \text{ keV}$. It is noteworthy that such situations can be easily established by irradiating a moderate-intensity laser light of $I_L \lambda_L^2 \geq 10^{16} \text{ W/cm}^2 - \mu\text{m}^2$ [14]. As for astrophysical aspects, the issue presented here is relevant to supernova outbursts [15].

The spherically symmetric fluid code has been developed on the Lagrangian frame $dm = 4\pi\rho r^2 dr$ with the specific volume of $V = \rho^{-1}$. This solves a set of two-temperature fluid equations for an ideal gas, including the relativistically corrected equations for the internal energy of electrons. That is,

$$\frac{du_i}{dt} = -4\pi r^2 \frac{\partial}{\partial m} (P_e + P_i + P_{ph}), \quad (1)$$

$$\frac{d(c_{ve_rel} T_e)}{dt} + P_e \frac{dV}{dt} = \frac{\partial}{\partial m} \left(4\pi r^2 \kappa_{e_rel} \frac{\partial T_e}{\partial r} \right) - \omega_{ei_rel} (T_e - T_i) - S_{brems} + S_{e_nucl} + S_L, \quad (2)$$

$$c_{vi} \frac{dT_i}{dt} + P_i \frac{dV}{dt} = \frac{\partial}{\partial m} \left(4\pi r^2 \kappa_i \frac{\partial T_i}{\partial r} \right) - \omega_{ei_rel} (T_i - T_e) + S_{i_nucl}. \quad (3)$$

Here, conventional abbreviations have been used. In particular, κ_{e_rel} , ω_{ei_rel} , and c_{ve_rel} denote the relativistic Spitzer-Härm heat conductivity [13], energy relaxation coefficient [16], and specific heat [17], respectively. These coefficients normalized by their nonrelativistic values are given by

$$\tilde{\kappa}_{e_rel}(\alpha) \equiv \frac{\kappa_{e_rel}(\alpha)}{\kappa_{e_nonrel}(\alpha)} = \frac{(2\pi)^{1/2}}{384} \frac{\alpha^{7/2}}{K_2(\alpha)} \left[\frac{\Theta_1^2(\alpha)}{\Theta_2(\alpha)} + \Theta_3(\alpha) \right], \quad (4)$$

$$\tilde{\omega}_{ei_rel}(\alpha) \equiv \frac{\omega_{ei_rel}(\alpha)}{\omega_{ei_nonrel}(\alpha)} = \frac{(2\pi)^{1/2}}{2} \frac{\exp(-\alpha)}{\alpha^{1/2} K_2(\alpha)} \left(1 + \frac{2}{\alpha} + \frac{2}{\alpha^2} \right), \quad (5)$$

$$\tilde{c}_{ve_rel}(\alpha) \equiv \frac{c_{ve_rel}(\alpha)}{c_{ve_nonrel}} = \frac{2}{3} \left[\alpha^2 + 5\alpha \frac{K_3(\alpha)}{K_2(\alpha)} - \alpha^2 \frac{K_3^2(\alpha)}{K_2^2(\alpha)} - 1 \right], \quad (6)$$

where $K_\nu(\alpha)$ is the modified Bessel function of index ν with its argument of $\alpha \equiv m_0 c^2 / T_e$, and the functions $\Theta_1(\alpha)$, $\Theta_2(\alpha)$, and $\Theta_3(\alpha)$ are defined by [18]

$$\Theta_1(\alpha) = \left(1 - \frac{1}{\alpha} + \frac{2}{\alpha^2} + \frac{42}{\alpha^3} + \frac{120}{\alpha^4} + \frac{120}{\alpha^5} \right) \exp(-\alpha) + \alpha \text{Ei}(-\alpha), \quad (7a)$$

$$\Theta_2(\alpha) = \left(1 - \frac{1}{\alpha} + \frac{2}{\alpha^2} - \frac{6}{\alpha^3} - \frac{24}{\alpha^4} - \frac{24}{\alpha^5} \right) \exp(-\alpha) + \alpha \text{Ei}(-\alpha), \quad (7b)$$

$$\Theta_3(\alpha) = \left(\frac{48}{\alpha^2} + \frac{288}{\alpha^3} + \frac{720}{\alpha^4} + \frac{720}{\alpha^5} \right) \exp(-\alpha), \quad (7c)$$

where $\text{Ei}(-\alpha)$ is the exponential integral function. The normalized coefficients (4)-(6) for

some α values are shown in Table I. Note that for $\alpha \gg 1$, eq. (4) asymptotically approaches unity, and for $\alpha \ll 1$, approaches the expression of $\tilde{\kappa}_e = [5(2\pi)^{1/2}/32]\alpha^{1/2}$ [18]. Another important point is that the heat capacity tends to increase in high-temperature regimes, up to twofold in the ultrarelativistic limit. Making use of the implicit finite differential scheme, we can numerically integrate the internal energy eqs. (2)-(7) as outlined in the Appendix.

In the LFFI context, of course, one can also construct some kinds of kinetic simulation codes [19] to investigate asymmetric transport involving magnetic fields [3, 9, 10], but their allowed spatiotemporal ranges are small. Regarding the present scheme, the macroscopic transport properties in *supersolid density* regions and the effects of a *more realistic plasma gradient* as well, can be revealed as a trade-off for missing the smaller spatiotemporal scales, such as the Debye length and the plasma oscillation period. Along the diffusion approximation adopted under geometrical constraint, irradiating laser intensity I_L is traced by $v_g(\partial I_L/\partial r) = -\nu_{abs}I_L$, where v_g and ν_{abs} denote the group velocity of light and the absorption coefficient, respectively [20]. For simplicity, in the present simulations, the laser light is set at normal incidence. The ray deposits its own energy, when propagating through the corona, and is then resonantly damped at the critical density. Note that in eq. (1) radiation pressure P_{ph} is also taken into account.

Furthermore, we are concerned with the thermonuclear reactions of deuterium-tritium (DT) and deuterium-deuterium (DD) fusion. The rate equations for number density of the tritium N_T and deuterium N_D [21] were solved in a postprocessing manner. Assuming the local self-heating due to charged particles, one obtains the source terms of eqs. (2) and (3) as functions of the heating power densities of $S_{DT} \propto \langle v\sigma_{DT} \rangle N_D N_T$ and $S_{DD} \propto \langle v\sigma_{DD} \rangle N_D^2$ [22]. Although these models are rather crude, they still have merit for the investigation of fundamental transport processes of electrons. As shown later, it is instructive to compare the neutron yields derived from various models of electron transport.

In the following, I demonstrate how a highly compressed fuel can be heated due to electron transport, and ignited. For convenience, 'case A' and 'case B' are used as references for simulations with and without relativistic effects, respectively. The initial laser conditions and target parameters are shown in Table II. Hereafter, the target parameters are fixed. The total mass of the target shell is on the order of that presented in ref. [23], and the initial aspect ratio of the shell is about $(R/\Delta R)_0 \sim 10$. High compression of the shell, maintaining a low entropy, is carried out by the Gaussian pulse shaping of driver laser light. The outer

thin ablator of carbonized DT (CDT) is blown off just before the deceleration phase, leaving the dense compressed core of DT fuel. Hydrodynamic instabilities concomitant with the low-entropy implosion are omitted for the moment.

In Fig. 1(a) for case A, I show a flow diagram of implosion with additional heating. The total mesh number is $J = 102$, and the flow lines are displayed each tenth mesh. At $t = 2.25$ ns, an additional 10 PW (10^{16} W) power with the pulse duration of $\tau = 1$ ps is deposited at a relativistically modified cut-off density which is defined by $n_{c_rel} = n_c \sqrt{1 + I_L \lambda_L^2 / (1.37 \times 10^{18} \text{ W/cm}^2 - \mu\text{m}^2)}$, where $n_c = 9.97 \times 10^{20} (1.06 \mu\text{m}/\lambda_L)^2 \text{ cm}^{-3}$ is the nonrelativistic cut-off density. In this case, the pulse intensity becomes about $I_L \lambda_L^2 \sim 10^{18} \text{ W/cm}^2 - \mu\text{m}^2$. One can see of the detonation shock propagating radially inwards, as well as the explosion, associated with the off-center fast ignition. The flow diagram without additional heating is shown in Fig. 1(b). It is confirmed that ignition does not occur in the standard implosion of the small target when using a driver laser energy of about 4 kJ.

The spatial profiles of plasma temperature and mass density at $t = 2.251$ ns, the moment that the additional heating power of 10 PW is switched off, are shown in Fig. 2 for cases A and B. One may notice that in the regions of $r = 0 - 35 \mu\text{m}$, the stagnating isobaric core where a central hot spot is surrounded with cold dense plasma (DT main fuel) is well established as a result of the low-entropy implosion. The equilibrium static pressure reaches $P = P_e + P_i > 10$ Gbar. It turns out that nonlinear propagation of the deflagration wave directly heats the main fuel. Here we define the average electron temperature of the main fuel as $\langle T_e \rangle = \int_{r_1}^{r_2} \rho T_e r^2 dr / \int_{r_1}^{r_2} \rho r^2 dr$, where r_1 and r_2 indicate the inner and outer radii where $\rho = \rho_{\text{peak}}/10$, respectively. In case B without relativistic corrections, the average temperature is $\langle T_e \rangle \simeq 9.9$ keV. On the other hand, in case A, the heat flux inhibition due to relativistic effects lowers the temperature to $\langle T_e \rangle \simeq 6.6$ keV. This reflects the factor $\tilde{\kappa}_e/\tilde{c}_{ve} \simeq 0.75$ for $T_e \simeq 25$ keV in the tenuous corona (see Table I). The relativistic effects on energy transfer between electrons and ions are small.

In Fig. 3 for case A, I show the spatial profiles of plasma temperature and mass density, just before the irradiation of the ignitor pulse ($t = 2.25$ ns), during the irradiation ($t = 2.2505$ ns), and just after the irradiation ($t = 2.251$ ns). While the coronal electrons are rapidly heated up to $T_e \sim 25$ keV, the deflagration wavefront slowly propagates in the cold dense region where the heat capacity is very large, and the steep temperature gradient at the wavefront self-generates a longitudinal electric field having a maximum value on the order

of magnitude of $E_{\max} \sim e^{-1} |\partial T_e / \partial r| \sim 10^{10}$ V/m [18]. For the plasma parameters shown in Figs. 2 and 3, the heating rate of the DT fuel ions is estimated to be $dT_i/dt \sim 1 - 1.5$ keV/ps, when assuming the Coulomb logarithm of $\ln \Lambda \sim 5$. The fuel can be, therefore, heated to the ignition temperature until the stagnating core is disassembled.

Let us show the additional heating power dependencies of neutron yields in Fig. 4 for both cases A and B. Within the range of 0.1 – 20 PW, an additional power with the pulse duration of $\tau = 1$ ps is injected at $t = 2.250$ ns. It is found that in the present model the threshold power for ignition seems to be about 1 PW, corresponding to the energy of 1 kJ. The pulse power of about 20 PW leads to a considerable increase in neutron yields, which are of the order of one thousand times that in the case without additional heating. The time-integrated bremsstrahlung loss is 60 – 70 J at most. It is noted that the flux inhibition degrades the heating efficiency, thereby reducing the neutron yields, particularly, when the additional power is, in this model, in the range of 3 – 10 PW. The yields tend to be sensitive to the timing of the irradiation of the ignitor pulse [24, 25].

The present predictions of the neutron yields and the threshold power for ignition may be rather pessimistic for determining the lower limit of the yields. In order to argue this point, I show, in Fig. 4, some results of the Fokker-Planck simulation coupled with spherically imploding hydrodynamics [24]. In this calculated example, the laser irradiation conditions and target parameters are similar to those presented in Table II. It is assumed that the absorbed energy of an ignitor pulse is transferred by 50 % into the high-energy tail electrons of the temperature (variance) of 50 keV. As shown in the figure, the effects of nonlocal transport seem to increase the neutron yields, since the hot tail electrons, which possess a longer mean-free path, deeply penetrate into the compressed plasma, preheating the fuel. It is noted that such nonlocality, as well as anisotropy of energy deposition, could be an advantage to the LFFI. The details should be clarified by multidimensional fluid simulations including relativistic kinetics in the future.

APPENDIX: IMPLICIT DIFFERENCE OF RELATIVISTICALLY CORRECTED INTERNAL ENERGY EQUATIONS

In this appendix, I briefly explain the numerical method to integrate the relativistically corrected energy equations. The implicit finite difference of eq. (2) can be cast to

$$\begin{aligned}
& \frac{c_{ve,j+1/2}^* T_{e,j+1/2}^* - c_{ve,j+1/2}^n T_{e,j+1/2}^n}{\Delta t^{n+1/2}} = -P_{e,j+1/2}^n \frac{V_{j+1/2}^{n+1} - V_{j+1/2}^n}{\Delta t^{n+1/2}} \\
& - \frac{4\pi}{\Delta m_{j+1/2}} \left[(1 - \phi) \left(\kappa_{e,j+1}^* r_{j+1}^2 \frac{T_{e,j+3/2}^* - T_{e,j+1/2}^*}{\Delta r_{j+1}^{n+1}} - \kappa_{e,j}^* r_j^2 \frac{T_{e,j+1/2}^* - T_{e,j-1/2}^*}{\Delta r_j^{n+1}} \right) \right. \\
& \quad \left. + \phi \left(\kappa_{e,j+1}^n r_{j+1}^2 \frac{T_{e,j+3/2}^n - T_{e,j+1/2}^n}{\Delta r_{j+1}^n} - \kappa_{e,j}^n r_j^2 \frac{T_{e,j+1/2}^n - T_{e,j-1/2}^n}{\Delta r_j^n} \right) \right] \\
& - (1 - \phi) \omega_{ei,j+1/2}^* (T_{e,j+1/2}^* - T_{i,j+1/2}^n) - \phi \omega_{ei,j+1/2}^n (T_{e,j+1/2}^n - T_{i,j+1/2}^n) + S_{j+1/2}^n, \quad (\text{A.1})
\end{aligned}$$

where r_j ($j = 0, 1, 2, \dots, J$) denotes the discrete positions of fluid elements and ϕ ($\leq 1/2$) is the implicit parameter, e.g., the Crank-Nicholson scheme corresponds to the case of $\phi = 1/2$. The last term on the right-hand side, $S_{j+1/2}^n$, represents generic power sources and/or sinks. Note that the coefficients κ_e , ω_{ei} , and c_{ve} depend upon the temperatures.

In the present simulation, the tridiagonal matrix (A.1) for $\phi = 0$ is inverted by the cyclic reduction method [26]. The temperature at the intermediate time steps $T_{e,j+1/2}^*$ and the coefficients involving this are iteratively advanced to the next ($T_{e,j+1/2}^{**}$). When the condition of $|T_{e,j+1/2}^{**} - T_{e,j+1/2}^*| / (T_{e,j+1/2}^{**} + T_{e,j+1/2}^*) < \epsilon$ ($\forall j$) is satisfied for a small value of ϵ , the vector $T_{e,j+1/2}^{**}$ is replaced by $T_{e,j+1/2}^{n+1}$. These procedures are repeated each time step, whose increment $\Delta t^{n+1/2}$ is automatically changed, invoking the Courant-Friedrich-Lewy condition.

-
- [1] N. J. Fisch: Rev. Mod. Phys. **59** (1987) 175.
 - [2] M. Tabak, J. Hammer, M. E. Glinsky, W. L. Kruer, S. C. Wilks, J. Woodworth, E. M. Campbell and M. D. Perry: Phys. Plasmas **1** (1994) 1626.
 - [3] A. Pukhov and J. Meyer-ter-Vehn: Phys. Rev. Lett. **79** (1997) 2686.
 - [4] R. J. Mason and M. Tabak: Phys. Rev. Lett. **80** (1998) 524.
 - [5] A. Caruso and V. A. Pais: Nucl. Fusion **36** (1996) 745.
 - [6] S. Atzeni and M. L. Ciampi: Nucl. Fusion **37** (1997) 1665.
 - [7] A. R. Piriz and M. M. Sanchez: Phys. Plasmas **5** (1998) 2721.
 - [8] A. R. Piriz and M. M. Sanchez: Phys. Plasmas **5** (1998) 4373.
 - [9] M. Honda, J. Meyer-ter-Vehn and A. Pukhov: Phys. Rev. Lett. **85** (2000) 2128.

- [10] Y. Sentoku, K. Mima, Z. M. Sheng, P. Kaw, K. Nishihara and K. Nishikawa: Phys. Rev. E, **65** (2002) 046408.
- [11] K. A. Tanaka, R. Kodama and H. Fujita: Phys. Plasmas **7** (2000) 2014.
- [12] R. Kodama, P. A. Norrey and K. Mima: Nature **412** (2001) 798.
- [13] M. Honda and K. Mima: J. Phys. Soc. Jpn **67** (1998) 3420.
- [14] M. Honda and K. Mima: Plasma Phys. Control. Fus. **40** (1998) 1887.
- [15] M. S. Longair: *High Energy Astrophysics* (Cambridge Univ., Cambridge, 1994) 2nd ed., Vol. 2.
- [16] S. T. Beliaev and G. I. Budker: Sov. Phys. Dokl. **1** (1956) 218.
- [17] R. Balescu and I. Paiva-Veretennicoff: Physica A **81** (1975) 17.
- [18] M. Honda: Phys. Plasmas **10** (2003) 4177.
- [19] A. Pukhov: J. Plasma Phys. **61** (1999) 425.
- [20] W. L. Kruer: *The Physics of Laser Plasma Interactions* (Wesley, California, 1988).
- [21] J. D. Huba: *NRL Plasma Formulary* (NRL, Washington DC, 1994).
- [22] J. J. Duderstadt and G. A. Moses: *Inertial Confinement Fusion* (Wiley, New York, 1982).
- [23] H. Azechi, T. Jitsuno and T. Kanabe: Laser Part. Beams **9** (1991) 193.
- [24] K. Mima, M. Honda, S. Miyamoto and S. Kato: *Proc. 12th Int. Conf. Laser Interaction and Related Plasma Phenomena, Osaka, 1995* (AIP, New York, 1996), Vol. 369, p.179.
- [25] R. Kodama and the Fast-Ignitor Consortium: Nature **418** (2002) 933.
- [26] W. H. Press, S. A. Teukolsky, W. T. Vetterling and B. P. Flannery: *Numerical Recipes Vol. 1, Fortran Numerical Recipes* (Cambridge Univ., Cambridge, 1992).

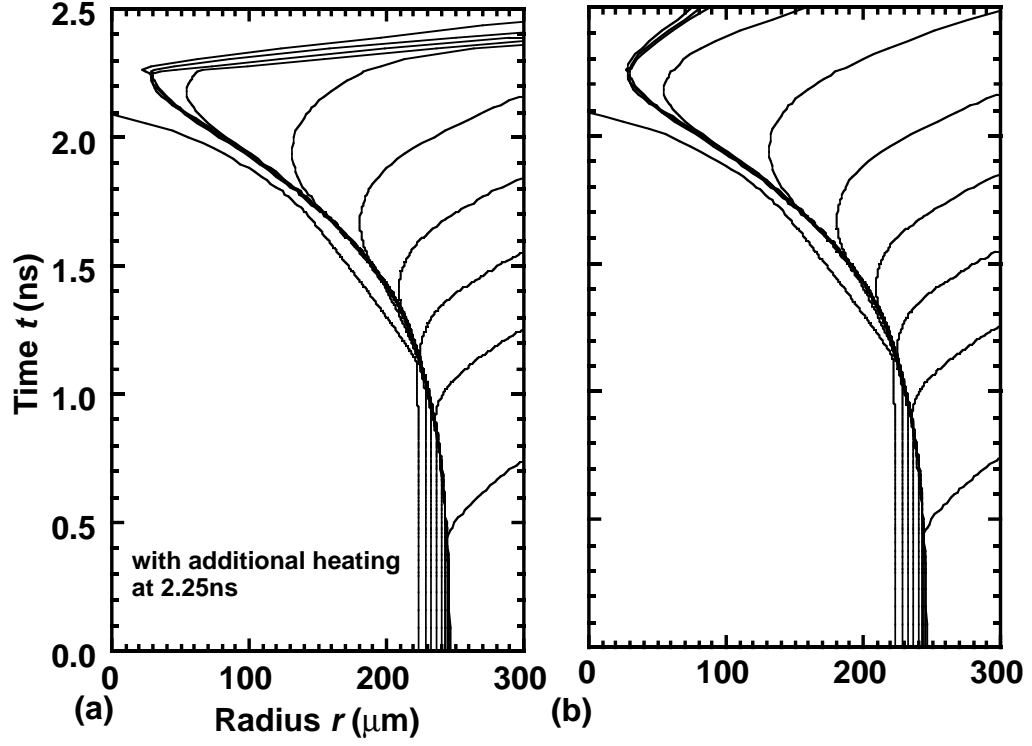


FIG. 1: Flow diagrams of laser implosion (a) with additional heating and (b) without additional heating. The figures have the same axes, and the flow lines are displayed each tenth mesh. At $t = 2.250$ ns for (a), the additional heating power of 10 PW having the pulse duration of $\tau = 1$ ps is deposited at the relativistically corrected critical surface.

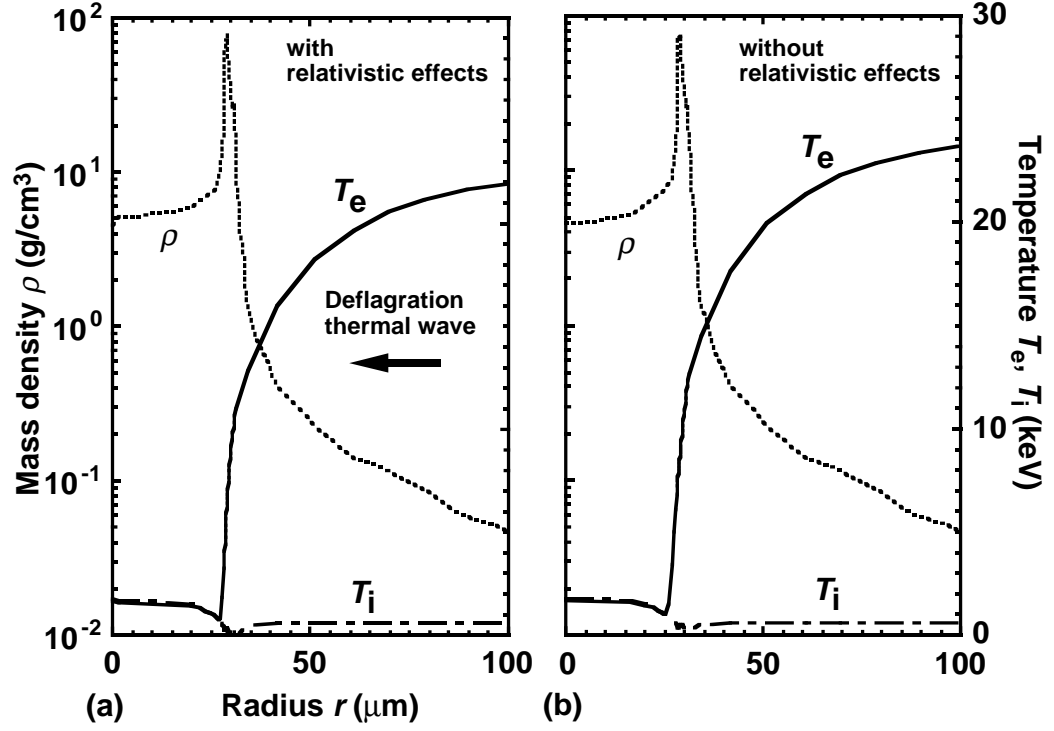


FIG. 2: The spatial profiles of electron temperature (full curves), ion temperature (dot-dashed curves), and mass density (dotted curves) at $t = 2.251$ ns (a) for case A with relativistic effects and (b) for case B without relativistic effects. The figures have the same axes.

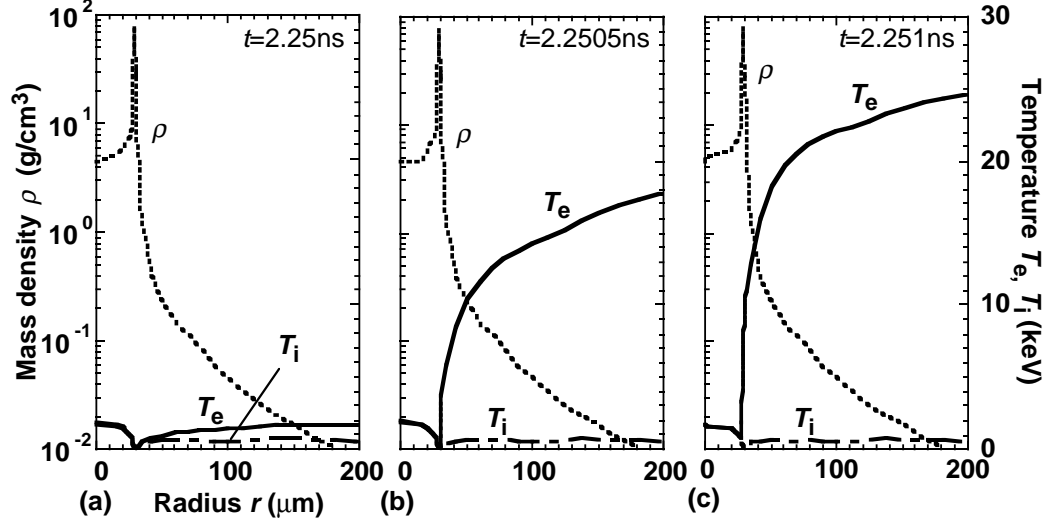


FIG. 3: The spatial profiles of electron temperature (full curves), ion temperature (dot-dashed curves), and mass density (dotted curves) for case A; (a) just before the pulse power injection, (b) during the injection of 10 PW, and (c) just after that. The figures have the same axes.

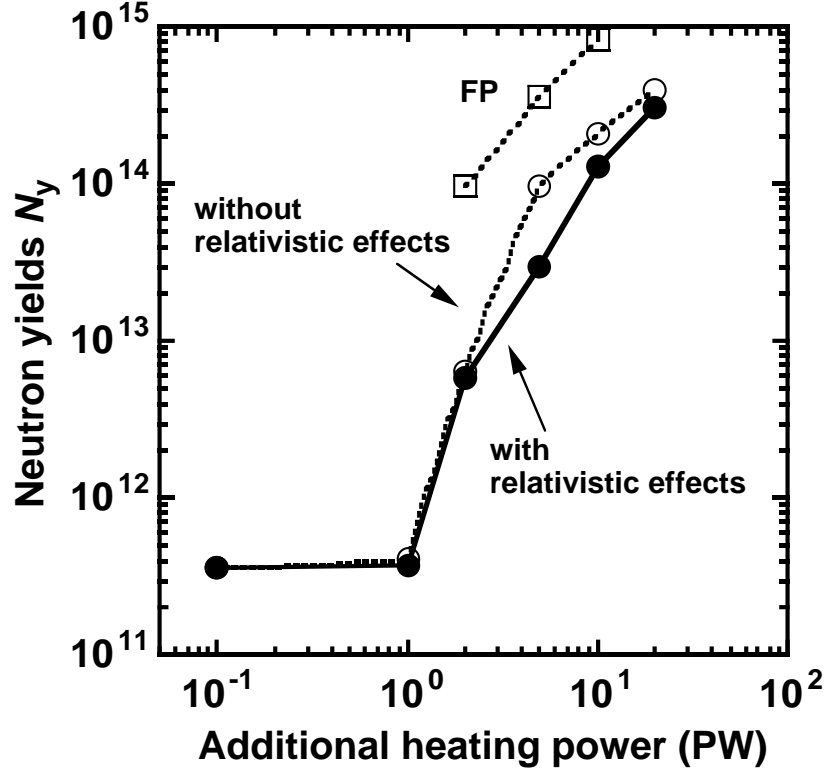


FIG. 4: Additional heating power dependencies of neutron yields. The full and open circles are for cases A and B, respectively. The target parameters and driver laser conditions for implosion are the same as those given in Table II. For comparison, the corresponding results of the Fokker-Planck (FP) simulation are also shown (open squares). For explanation see text.

TABLE I: The relativistic correction factors given by eqs. (4)-(7) in the text.

α	T_e (MeV)	$\tilde{\kappa}_e^a$	$\tilde{\omega}_{ei}^b$	\tilde{c}_{ve}^c	$\tilde{\kappa}_e/\tilde{c}_{ve}$
$\ll 1$	—	—	—	2	—
0.05	10.2	0.087556	5.6084	1.9992	0.043796
0.1	5.11	0.12373	3.9726	1.9968	0.061966
0.5	1.02	0.27123	1.8510	1.9393	0.13986
1	0.511	0.36792	1.4188	1.8343	0.20058
5	0.102	0.62668	1.0528	1.3746	0.45589
10	0.0511	0.73598	1.0206	1.2156	0.60546
20	0.0256	0.83044	1.0084	1.1160	0.74420
$\gg 1$	—	1	1	1	1

^aCited from ref. [13] by Honda and Mima.

^bCited from ref. [16] by Beliaev and Budker.

^cCited from ref. [17] by Balescu and Paiva-Veretennicoff.

TABLE II: Simulation parameters of laser implosion including additional heating.

Laser conditions			Target parameters	
	Driver pulse	Ignitor pulse		
Pulse shape:	Gaussian	Square	Inner radius:	223.32 μm (vacuum)
Laser energy:	4.1 kJ	10 kJ ^a	D _{0.5} T _{0.5} :	2.00 μm (3 meshes)
Wavelength:	0.53 μm	1.06 μm	D _{0.5} T _{0.5} :	16.92 μm (42 meshes)
Rise time:	0.6 ns ^b	—	C _{0.426} D _{0.534} T _{0.0153} :	4.76 μm (57 meshes)
Pulse width:	1.909 ns ^c	1.0 ps ^d		
Fall time:	0.5 ns ^e	—		
Peak power:	2.5 TW	10 PW ^a		

^aVariable between 0.1 kJ–20 kJ (100 TW–20 PW), as seen in Fig. 4.

^bIt follows the Gaussian pedestal of 1.2 ns.

^cFWHM, including the top flat part of 0.809 ns.

^dSwitched on at $t = 2.250$ ns.

^eAdditional Gaussian pedestal of 1.0 ns follows its fall.